Am J Nucl Med Mol Imaging 2026;16(3):131-142
www.ajnmmi.us /ISSN:2160-8407/ajnmmi0173111

Original Article

Evaluation of albumin-binding PD-L1-targeted VHH for PET imaging in colorectal cancer

Rui Zhang[1*], Jun Li[2*], Ping Chen[3*], Mengjie Dong[2], Ling Ding[1]

[1]Department of Epidemiology, School of Public Health, Shanxi Medical University, Taiyuan, Shanxi, China; [2]Department of Nuclear Medicine, Peking University Shenzhen Hospital, Shenzhen, Guangdong, China; [3]Department of Pharmacy, Peking University Shenzhen Hospital, Shenzhen, Guangdong, China. [*]Co-first authors.

Received April 6, 2026; Accepted May 8, 2026; Epub June 15, 2026; Published June 30, 2026

Abstract: Objective: Immunotherapy plays a pivotal role in the treatment of colorectal cancer (CRC). PD-L1 has been identified to be a significant biomarker of response to treatment. The assessment of PD-L1 presently depends on biopsy samples - a problem that may be resolved with the help of a molecular imaging approach. This study devised and evaluated an ^{18}F-and ^{89}Zr-labelled albumin-binding PD-L1-targeted VHH for potential diagnostic imaging in CRC models. Methods: PD-L1 expression was initially validated in HCT-116 cell-derived xenografts and CRC20-PDX tumors. An albumin-binding moiety was conjugated to a PD-L1-targeted VHH to construct SN-2D01. The ^{18}F-labeled SN-2D01 was prepared using the AlF-RESCA chelation strategy and the probe was modified with DFO for a ^{89}Zr radiolabeling process. The evaluation of [^{18}F]F-SN-2D01 and [^{89}Zr]Zr-SN-2D01 through PET imaging was performed on the two tumor models and a quantitative analysis of tumor uptake for each tracer. Ultimately, a biodistribution study of [^{89}Zr]Zr-SN-2D01 at 120 h post-injection (p.i.) was performed in both tumor models. Results: The HCT-116 cell-derived xenografts and CRC20-PDX tumors were both PD-L1-positive, with a higher expression observed in lesions from CRC20-PDX versus HCT-116 tumors. The 2 h p.i. of [^{18}F]F-SN-2D01 PET showed clear visualization of HCT-116 and CRC20-PDX tumors, with tracer mostly cleared via hepatic and renal excretion. In PET imaging with [^{89}Zr]Zr-SN-2D01, the tumor uptake in both HCT-116 and CRC20-PDX slowly increased from 24 h to 120 h p.i, which peaked at 120 h. Biodistribution at 120 h showed tumor uptake of 11.49 ± 1.32 %ID/g for the CRC20-PDX model and 8.12 ± 1.54 %ID/g for the HCT-116 model. Conclusion: In summary, we presented two PET probes to visualize PD-L1. Of these, [^{89}Zr]Zr-SN-2D01 was found to have significant capability to evaluate PD-L1 expression in CRC. The PD-L1-targeted SN-2D01 may provide a new approach in radionuclide therapy targeting PD-L1 in CRC.

Keywords: PD-L1, colorectal cancer, immuno-PET, VHH-ABD

Introduction

Colorectal cancer (CRC) is the third most common cancer and the second most leading cause of cancer death globally [1-3]. The clinical management of CRC currently consists of a multi-disciplinary framework comprising surgical resection, conventional chemotherapy, radiotherapy (RT) and molecular targeted therapy [4, 5]. Over the last ten years there has been marked improvement in these treatment regimens [6-8]. Nevertheless, the worldwide death rate for CRC remains unacceptably high and incidence is roughly 915880 deaths per year, which is responsible for about 9.4% of the total cancer deaths [9]. Recently, due to the durable antitumor efficacy of immunotherapy, it has become a transformative paradigm in oncology, and its rapid clinical development has revolutionized the treatment landscape for CRC [10, 11]. According to its genetic characteristics, CRC comprises mismatch repair-deficient/microsatellite instability-high (dMMR/MSI-H) and mismatch repair-proficient/microsatellite instability-low (pMMR/non-MSI-H) disease [12, 13]. A number of landmark clinical trials have established that immune checkpoint inhibitors (ICIs) can elicit strong and durable clinical benefit in patients with dMMR/MSI-H CRC. Food and Drug Administration (FDA) has approved several ICIs including nivolumab and pembrolizumab for the treatment of this patient population [14-16].

The detection of PD-L1 expression levels in patient lesions enables clinicians to select candidates for immunotherapy rationally and predict treatment responses to PD-1/PD-L1 blockade. Currently, PD-L1 expression is routinely evaluated through immunohistochemical (IHC) analysis of tumor biopsy specimens, with the resulting PD-L1 expression score serving as a key eligibility criterion for PD-1/PD-L1 targeted therapy [17, 18]. However, IHC-based assessment is invasive and inherently limited by the pronounced spatiotemporal heterogeneity of PD-L1 expression within tumors, which precludes reliable dynamic monitoring during the treatment course [19]. The development of PD-L1-targeted radiotracers has opened new avenues for whole-body positron emission tomography (PET) imaging, allowing for non-invasive, repeatable, and real-time quantitative characterization of heterogeneous PD-L1 expression across the entire tumor burden [19, 20].

Numerous radiolabeled anti-PD-L1 antibodies and peptides have been studied for the development of PET

https://doi.org/10.62347/GBVO2400

probes for PD-L1 evaluation [21-28]. Nanobodies (Nbs), also called VHHs, are derived from the variable domains of the heavy-chain-only antibodies found in camelids and serve as excellent targeting scaffolds. Compared to classic monoclonal antibodies, nanobodies possess strong target binding affinity and specificity, smaller size, easy production, and high flexibility for genetic engineering or conjugating with chemicals. Having a molecular weight of around 15 kDa, they have fast penetration and elimination from tissues and kidneys, resulting in favourable pharmacokinetics and high-contrast image quality [29, 30]. Several PD-L1-targeting tracers based on VHHs have entered into clinical trials [31-33].

Targeted radionuclide therapy (TRT) is a clinically established therapeutic modality [34]. While VHHs exhibit favorable imaging characteristics, these same properties can limit tumor accumulation and consequently reduce the radiation dose delivered for therapeutic purposes [35]. Furthermore, the kidneys remain the primary dose-limiting organ in VHH-based treatments, highlighting the urgent need to optimize the pharmacokinetic profiles of VHH constructs [36]. Extensive studies have demonstrated that albumin binding can effectively enhance tumor uptake while mitigating renal radiation burden. Notably, to date, no studies have reported on PET imaging utilizing PD-L1-targeted VHH-ABD constructs. In this context, we propose to radiolabel the PD-L1-targeting VHH-ABD agent SN-2D01 with two diagnostic radionuclides: ^{18}F and ^{89}Zr. The in vivo biodistribution of [18F]F-SN-2D01 and [89Zr]Zr-SN-2D01 will be investigated in CRC models, with the aim of providing preclinical evidence and a reference for future PD-L1-directed TRT in CRC.

Materials and methods

Reagents, cell lines, and animal models

The anti-human PD-L1 ABD-VHH (SN-2D01) was supplied by Shenzhen Shennan Coupling Biomedical Technology Co., Ltd. The colorectal cancer cell line HCT-116 was obtained from Procell Life Science & Technology Co., Ltd. The tumor models were prepared using cell culture and standard preparation methods as per routine.

All animal procedures were performed in accordance with the protocols approved by the Animal Ethics Committee of Shenzhen PKU-HKUST Medical Center (approval no. 2023-631). 4-6 weeks old female Balb/c-Nude mice were sourced from Gempharmatech Co., Ltd. For establishing subcutaneous xenograft models, a mixture of 3-5 × 10^6 tumour cells was suspended with 100-200 μL of PBS and inoculated subcutaneously in the mice.

The human colorectal cancer biopsy-derived tissue was implanted into the flank of 5-week-old female Balb/c-Nude mice to establish CRC20 patient-derived xenograft (PDX) model.

Immunohistochemical staining for PD-L1

Tissues from CRC models were collected, and the tissue slides were stained with an anti-PD-L1 antibody (GB155736-100, Servicebio, 1:200). In order to block endogenous peroxidase activity, the sections were subjected to microwave treatment for three cycles of 5-10 min, which was then followed by incubation with 3% hydrogen peroxide for 15 min at room temperature. The sections were washed in PBS and incubated with the secondary antibodies at room temperature for 1 hr. Following washing, a 1:200 dilution of HRP-conjugated rabbit-specific secondary antibody was applied for 50 min at room temperature. The immunoreactivity was observed by 3,3'-diaminobenzidine for 5 min, and then these sections are counter-stained with Mayer's hematoxylin for 15 min before rinsing with distilled water.

RESCA conjugation and ^{18}F-labeling of SN-2D01

For preparation prior to radiolabeling, PD-10 columns were pre-equilibrated with 10 mL of 0.05 M $NaHCO_3$ solution (pH 8.6). Subsequently, 5 mg SN-2D01 (in PBS buffer) was loaded onto the PD-10 column, and the volume was made up to 2.5 mL with the same 0.05 M $NaHCO_3$ buffer. The eluate was then collected with a further 2.5 mL 0.05 M $NaHCO_3$ solution which was retained for further conjugation.

(±)H3RESCA-TFP (BDDH-1, 25 mg; Confluore Biological Technology) was weighed in a molar ratio of 12:1 relative to SN-2D01 followed by dissolving in 30 μL of DMSO. The SN-2D01 solution was mixed with the dissolved (±) H3RESCA-TFP. The conjugation reaction was carried out at room temperature for 2 h under continuous shaking. The resulting mixture was then applied to a pre-equilibrated PD-10 column and eluted with 0.1 M CH_3COONH_4 solution (pH 4.6). The collected eluate was concentrated using a 10 kDa molecular weight cut-off ultrafiltration tube (Merck). The purified RESCA-SN-2D01 conjugate was kept at -20°C until use in radiolabelling experiments.

For ^{18}F-labeling, the QMA cartridge was preconditioned sequentially with 5 mL of sterile water for injection, 5 mL of air, 5 mL of 0.9% saline, and a final 5 mL of air. Cyclotron-produced enriched ^{18}F in 500 μL of water was then passed through the QMA cartridge, and the filtrate was discarded. Subsequently, 500 μL of 0.9% saline was introduced into the cartridge, and this collection step was repeated twice, yielding a measured activity of 555 MBq. Thereafter, 8 μL of 2 mM $AlCl_3$ solution was added, mixed thoroughly, and allowed to stand for 5 min. Next, 200-300 μg of RESCA-SN-2D01 was added sequentially together with 100 μL of 0.1 M CH_3COONH_4 solution. The labeling reaction was allowed to proceed at room temperature for 12 min.

Meanwhile, a PD-10 column was pre-equilibrated with 10 mL of phosphate-buffered saline (PBS). The reaction

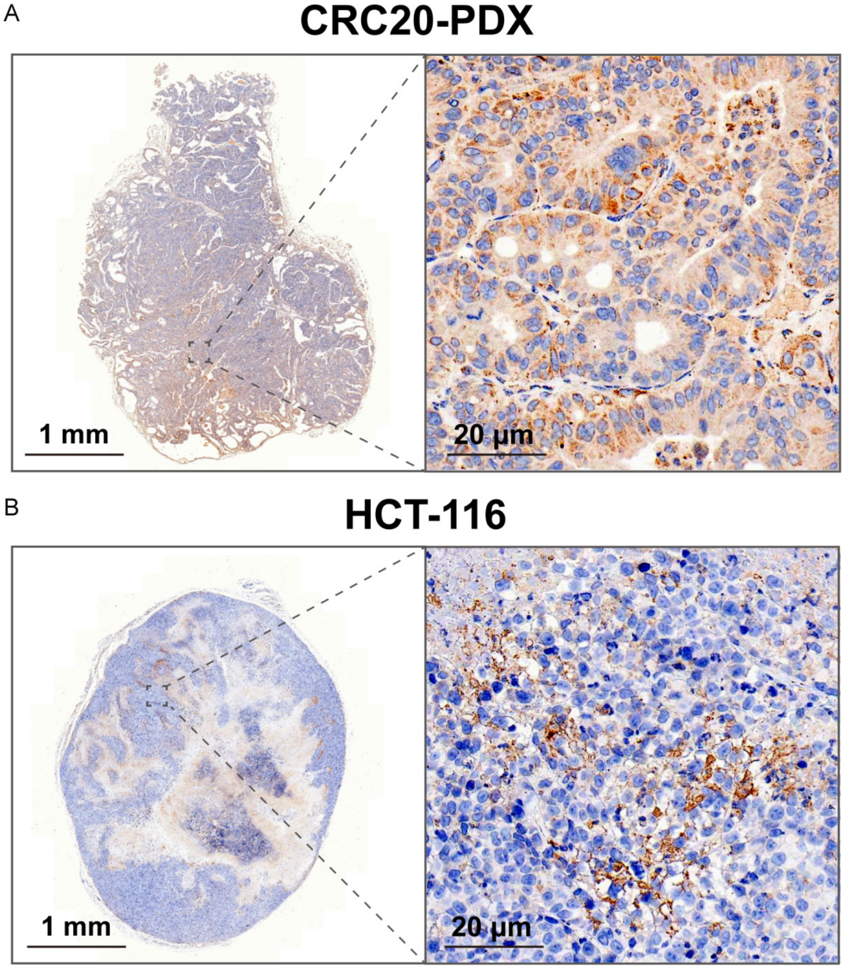

Figure 1. Immunohistochemical analysis of PD-L1 expression in CRC20-PDX and HCT-116 tumors. A. Representative images of PD-L1 staining in CRC20-PDX tumor tissue. B. Representative images of PD-L1 staining in HCT-116 tumor tissue. Dashed boxes denote regions of interest that are presented at higher magnification. Scale bars represent 1 mm in low-magnification images and 20 μm in high-magnification images.

mixture was loaded onto the PD-10 column and adjusted to a final volume of 2.5 mL using the elution buffer. Elution was then performed by collecting 0.5 mL fractions into five separate tubes, and the radioactivity of each fraction was measured individually. The radiochemical purity (RCP) of the final product was determined by iTLC.

DFO conjugation and ^{89}Zr labeling of SN-2D01

A phosphate buffered saline (PBS) solution containing 2-4 mg SN-2D01 was prepared. The pH of the solution was adjusted to 8.9-9.1 by 0.1 M Na_2CO_3 buffer (pH 11.4). DFO were freshly prepared by dissolving it in DMSO and adding it to the SN-2D01 solution at a molar ratio of 5:1 (DFO: SN-2D01). Reaction for the conjugation was performed at room temperature for 45 min with gentle agitation. Subsequently, the reaction mixture was purified on a PD-10 desalting column (GE Healthcare) using PBS as the eluent. The conjugate was then concentrated using a 10 kDa ultrafiltration tube (Merck).

The fresh ^{89}Zr for the radiolabeling was purchased from Guangdong Sinotau Molecular Imaging Technology Co., Ltd. In brief, ^{89}Zr-oxalic acid solution (20 μL, 74 MBq) was first neutralized with 2-3 μL of 1 M Na_2CO_3 buffer to adjust the pH to 7.1-7.3. Next, 200 μL of DFO-SN-2D01 solution (200-300 μg) was placed in the reaction vial. The labeling reaction proceeded at room temperature for 1 h with mild shaking. The final ^{89}Zr-labeled product was purified by a PD-10 column and the thin-layer chromatography (TLC) was applied to determine radio chemical purity (RCP).

In vivo imaging studies

Small-animal imaging studies were conducted in mice bearing CRC20-PDX or HCT-116 tumors (n = 3 per group) at Shenzhen Bay Laboratory/Bay Imaging Technology Company, China. Approximately 7.4 MBq of [^{18}F]F-SN-2D01 and 3.7 MBq of [^{89}Zr]Zr-SN-2D01 were injected via the tail vein for PET Imaging. During image acquisition, mice were anesthetized with 2.0%-2.5% isoflurane. Static scans were acquired at the designated time points post-injection. PET and PET/CT images were reconstructed using a three-dimensional ordered subset expectation maximization (3D OSEM) algorithm. Regions of interest (ROIs) were manually delineated using PMOD software (PMOD Technologies LLC, Zurich, Switzerland). Quantitative analysis was performed by normalizing ROI-derived activity to the injected dose, and tracer uptake was expressed as percentage injected dose per gram of tissue (%ID/g).

Biodistribution study

Ex vivo biodistribution studies were carried out in CRC20-PDX and HCT-116 tumor-bearing mice (n = 3 per group). Each mouse was intravenously injected with [^{89}Zr]Zr-SN-2D01. At 120 h post-injection, the mice were euthanized and major tissues, including blood, liver, heart, kidneys, lungs, spleen, stomach, small intestine, large intestine, pancreas, muscle, bone, and tumor, were collected. All samples were weighed and measured using a γ-counter, and the results were expressed as percentage of injected dose per gram of tissue (%ID/g).

Statistical analysis

Quantitative data are expressed as mean ± standard deviation (SD). Statistical analysis was carried out using

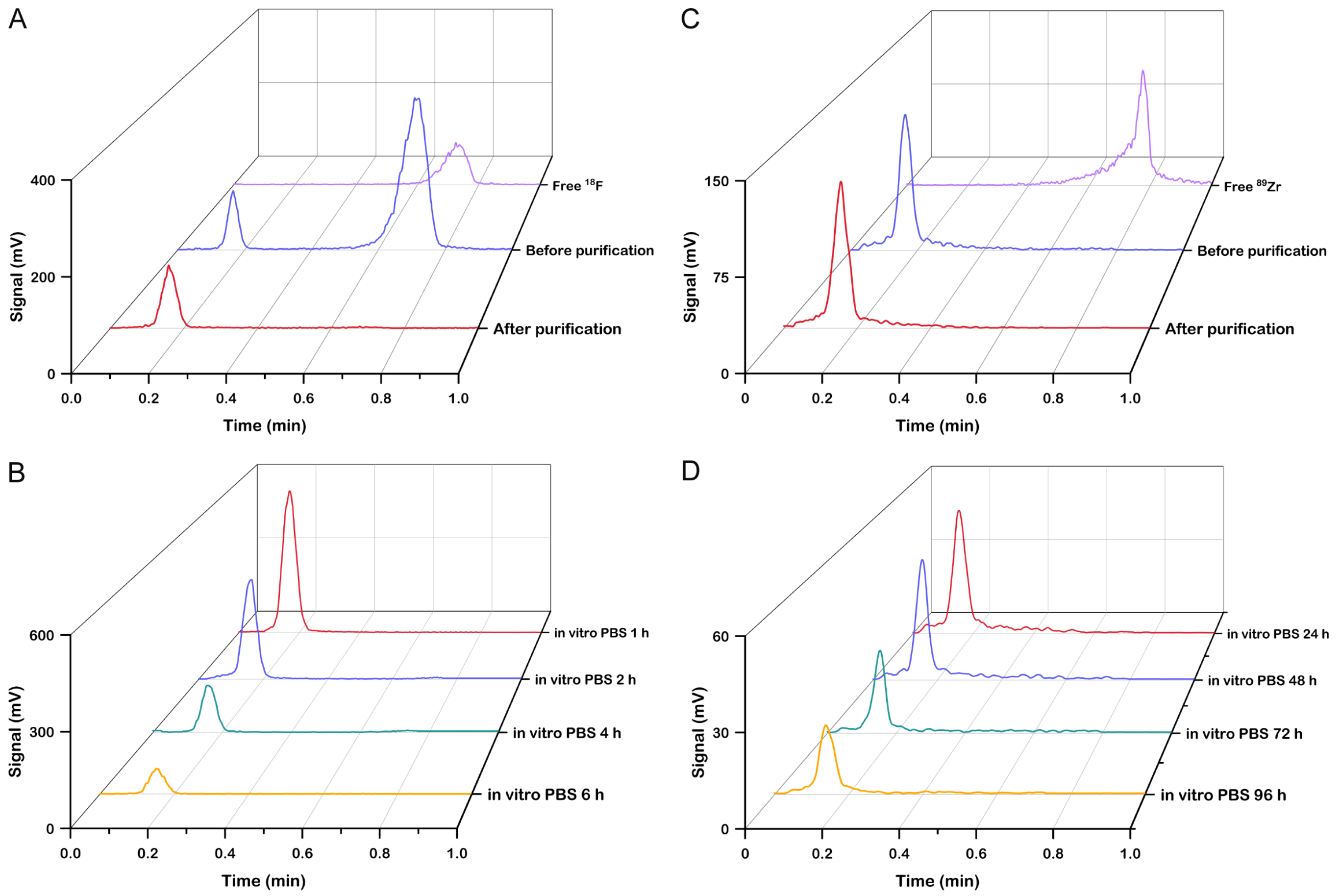

Figure 2. Characterization of [^{18}F]F-SN-2D01 and [^{89}Zr]Zr-SN-2D01. A. iTLC analysis of [^{18}F]F-SN-2D01. B. iTLC analysis of [^{89}Zr]Zr-SN-2D01. C. *In vitro* stability of [^{18}F]F-SN-2D01. D. *In vitro* stability of [^{89}Zr]Zr-SN-2D01.

GraphPad Prism (version 9). Comparisons between two groups were conducted using an unpaired Student's t-test. Differences were considered statistically significant when $P < 0.05$.*$P < 0.05$; **$P < 0.01$; ***$P < 0.001$.

Results

PD-L1 expression in CRC tumor models

Immunohistochemical staining was performed to assess PD-L1 expression in CRC20-PDX and HCT-116 tumor tissues. As presented in **Figure 1A**, **1B**, positive PD-L1 staining was observed in both models. The staining intensity was more pronounced in CRC20-PDX tumors than in HCT-116 tumors, indicating relatively higher PD-L1 expression in CRC20-PDX tissues.

Synthesis, radiochemistry, and stability

Radiolabeling of SN-2D01 with ^{18}F and ^{89}Zr was accomplished. The average radiochemical yield of [^{18}F]F-SN-2D01 was 79.34 ± 3.1% (n = 3), while [^{89}Zr]Zr-SN-2D01 was obtained with a radiochemical yield of 52.61 ± 3.46% (n = 3). The molar activity of [^{18}F]F-SN-2D01 was 68.70 ± 4.77 GBq/μmol, while that of [^{89}Zr]Zr-SN-2D01 was 80.87 ± 2.78 GBq/μmol. As shown in **Figure 2A** and **2B**, both tracers were prepared with high radiochemical purity, exceeding 98%. Their in vitro stability was further evaluated in PBS at 37°C. [^{18}F]F-SN-2D01 maintained an RCP above 95% after 6 h of incubation, while the RCP of [^{89}Zr]Zr-SN-2D01 remained above 95% after 96 h (**Figure 2C** and **2D**).

Micro-PET imaging of [^{18}F]F-SN-2D01 in HCT-116 tumor-bearing mice

Representative PET images showed that [^{18}F]F-SN-2D01 accumulated in HCT-116 tumors and that the tumor signal became progressively more prominent from 1 to 6 h p.i. (**Figure 3A**). Quantitative ROI analysis further demonstrated a time-dependent increase in tracer uptake in the tumor, with values rising from 2.01 ± 0.66 %ID/g at 1 h to 6.79 ± 0.67 %ID/g at 6 h p.i. (**Figure 3B**). Among the major tissues analyzed, the highest activity was observed in the heart, followed by the liver and kidneys, whereas muscle uptake remained low throughout the imaging period. At 6 h p.i., tracer uptake in the heart, liver, kidney, tumor, and muscle was 14.43 ± 0.40, 9.31 ± 0.77, 7.29 ± 0.77, 6.79 ± 0.67, and 1.90 ± 0.04 %ID/g, respectively. In addition, the tumor-to-muscle ratio increased gradually over time, from 2.89 ± 0.78 at 1 h to 3.93 ± 0.88 at 6 h

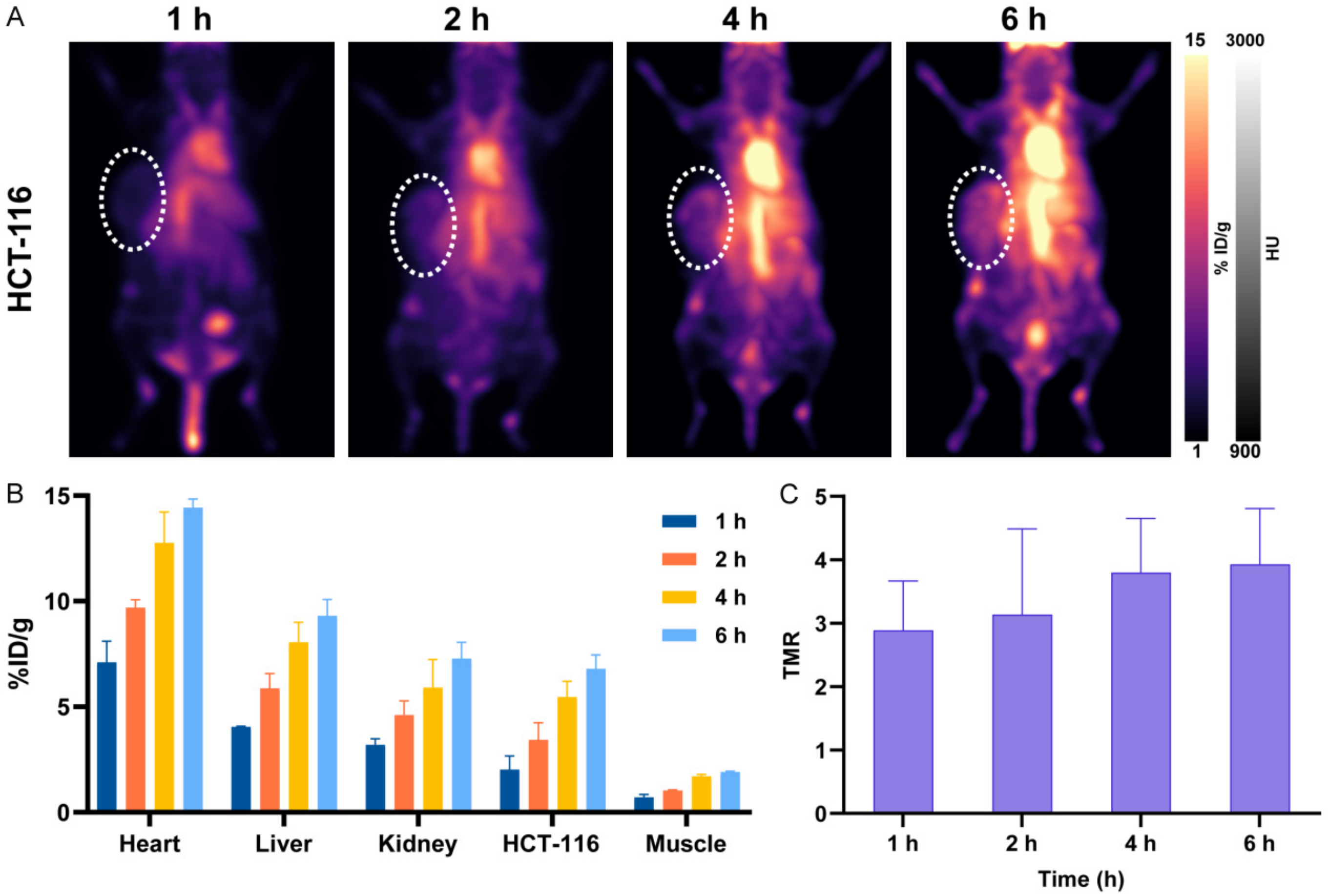

Figure 3. Micro-PET imaging of [^{18}F]F-SN-2D01 in the HCT-116 tumor model. A. Representative micro-PET images of [^{18}F]F-SN-2D01 in HCT-116 tumor-bearing mice at 1, 2, 4, and 6 h post-injection (p.i.). B. ROI analysis of [^{18}F]F-SN-2D01 uptake in HCT-116 tumor model. C. Tumor-to-muscle ratio (TMR) of [^{18}F]F-SN-2D01 in the HCT-116 tumor model.

p.i. (**Figure 3C**), indicating improved tumor contrast at later time points.

Micro-PET imaging of [^{18}F]F-SN-2D01 in CRC20-PDX tumors

The [^{18}F]F-SN-2D01 PET imaging showed stronger tumor uptake in CRC20-PDX-bearing mice compared to HCT-116 bearing mice (**Figure 4**), which is consistent with the stronger PD-L1 immunohistochemical staining in CRC20-PDX model. Representative images showed clear tracer accumulation in the CRC20-PDX tumors as early as 1 h p.i., with tumor uptake becoming progressively more intense at 2, 4, and 6 h p.i. (**Figure 4A**). Quantitative analysis further confirmed a time-dependent increase in tumor uptake, reaching 6.79 ± 0.67 %ID/g at 6 h p.i. Among the major organs analyzed, relatively high activity was observed in the heart, liver, and kidneys, whereas uptake in muscle remained low throughout the imaging period (**Figure 4B**). As a result, the tumor-to-muscle ratio gradually increased over time and reached 3.56 ± 0.27 at 6 h p.i., indicating improved tumor contrast at later time points (**Figure 4C**). Compared with the HCT-116 model, CRC20-PDX showed higher tumor-associated signal and more favorable tumor-to-background contrast, which was in agreement with its stronger PD-L1-positive staining. This trend is also consistent with previous PD-L1-targeted PET studies showing that tracer accumulation in tumors generally parallels PD-L1 expression levels and that contrast improves over time as background activity clears.

[^{89}Zr]Zr-SN-2D01 immuno-PET/CT imaging in HCT-116 tumors

[^{89}Zr]Zr-SN-2D01 PET/CT imaging enabled clear visualization of HCT-116 tumors from 24 to 120 h p.i. (**Figure 5A**). Quantitative analysis showed that tracer uptake in the tumor increased steadily over time, from approximately 6.71 ± 0.73 %ID/g at 24 h to 7.62 ± 0.32, 8.34 ± 0.59 %ID/g, 8.78 ± 0.34 %ID/g, and 9.37 ± 0.76 %ID/g at 48, 72, 96, and 120 h p.i., respectively (**Figure 5B**). Among the normal organs, the liver exhibited the highest uptake throughout the entire imaging period, with values rising gradually from about 14.90 ± 0.88 %ID/g at 24 h to 15.77 ± 0.21 %ID/g, 16.47 ± 0.71 %ID/g, 17.78 ± 1.41 %ID/g, and 18.30 ± 1.32 %ID/g at the subsequent time points. In contrast, heart uptake decreased continuously over time, dropping from approximately 6.63 ± 0.22 %ID/g at 24 h to 4.97 ± 0.59, 4.80 ± 0.57, 3.43 ± 0.15, and 3.06

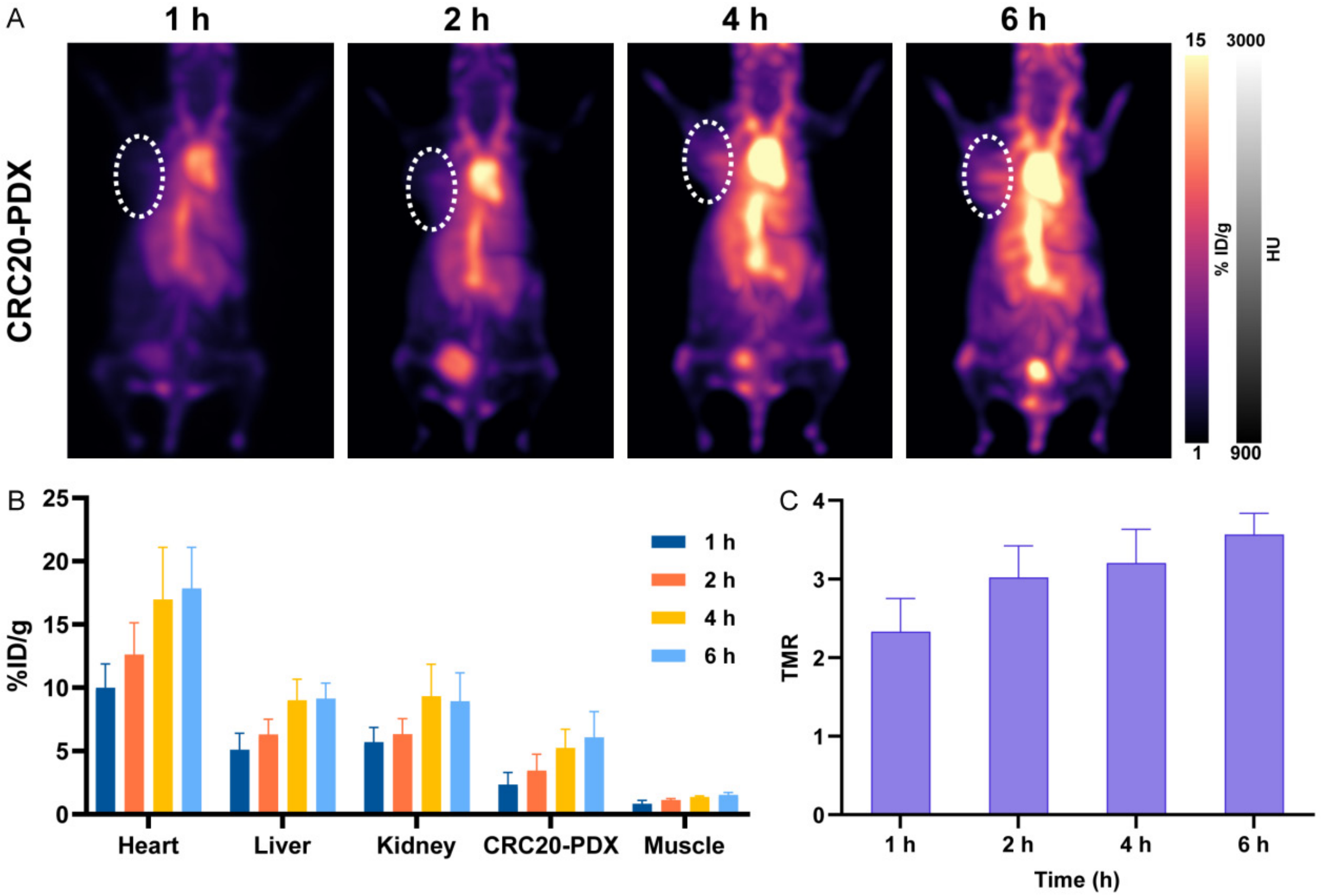

Figure 4. Micro-PET imaging of [^{18}F]F-SN-2D01 in the CRC20-PDX tumor model. A. Representative micro-PET images of [^{18}F]F-SN-2D01 inCRC20-PDX tumor-bearing mice at 1, 2, 4, and 6 h post-injection (p.i.). B. ROI analysis of [^{18}F]F-SN-2D01 uptake in CRC20-PDX tumor model. C. Tumor-to-muscle ratio (TMR) of [^{18}F]F-SN-2D01 in the CRC20-PDX tumor model.

± 0.33 %ID/g at 48, 72, 96, and 120 h p.i., respectively. Kidney uptake remained at a moderate level and showed only limited fluctuation during the observation period, measuring about 6.93 ± 0.22, 6.74 ± 0.10, 7.38 ± 1.25, 6.74 ± 0.76, and 7.68 ± 0.38 %ID/g from 24 to 120 h p.i. Muscle uptake was consistently low at all time points, remaining around 1 %ID/g or lower. As a result, the tumor-to-muscle ratio increased progressively from approximately 6.46 ± 0.60 at 24 h to 6.80 ± 0.44 at 48 h, 7.39 ± 0.95 at 72 h, 10.06 ± 0.87 at 96 h, and 10.99 ± 2.44 at 120 h p.i. (**Figure 5C**), with significantly higher values observed at 96 ($P < 0.05$) and 120 h ($P < 0.001$) compared with 24 h, indicating a continuous improvement in tumor contrast on delayed imaging. Collectively, these results showed persistent tumor retention of [^{89}Zr]Zr-SN-2D01 in the HCT-116 model, accompanied by decreasing background signal in some tissues and favorable tumor delineation at later time points.

[^{89}Zr]Zr-SN-2D01 immuno-PET/CT imaging in CRC20-PDX tumors

Similar to the findings in the HCT-116 model, [^{89}Zr]Zr-SN-2D01 PET/CT imaging enabled clear visualization of CRC20-PDX tumors from 24 to 120 h p.i. (**Figure 6A**). Quantitative analysis showed that tracer uptake in the CRC20-PDX tumors gradually increased over time, from 5.93 ± 0.38 %ID/g at 24 h to 6.46 ± 1.26, 8.18 ± 1.73, 8.40 ± 1.55, and 8.55 ± 2.18 %ID/g at 48, 72, 96, and 120 h p.i., respectively (**Figure 6B**). Among the major normal tissues, the liver showed the highest uptake throughout the imaging period, with values of 8.34 ± 0.95, 8.82 ± 1.89, 9.93 ± 1.68, 11.20 ± 3.69, and 12.20 ± 3.97 %ID/g at 24, 48, 72, 96, and 120 h p.i., respectively. In contrast, heart uptake decreased progressively over time, from 8.13 ± 1.75 %ID/g at 24 h to 5.83 ± 1.22, 5.28 ± 1.25, 4.30 ± 1.18, and 4.23 ± 1.28 %ID/g at the subsequent time points. Kidney uptake remained at a moderate level and exhibited only limited variation during the observation period, with values of 6.44 ± 1.20, 5.88 ± 0.90, 6.57 ± 1.21, 6.27 ± 1.24, and 6.96 ± 0.57 %ID/g from 24 to 120 h p.i. Muscle uptake remained low at all examined time points. Accordingly, the tumor-to-muscle ratio increased continuously from 4.54 ± 0.23 at 24 h to 6.14 ± 0.56, 7.93 ± 1.22, 8.26 ± 1.24, and 9.57 ± 2.28 at 48, 72, 96, and 120 h p.i., respectively (**Figure 6C**), with siginificantly higher values observed at 72 ($P < 0.01$), 96 ($P < 0.01$), and 120 h ($P < 0.001$) compared with 24 h, indicating progressive improvement in tumor contrast on

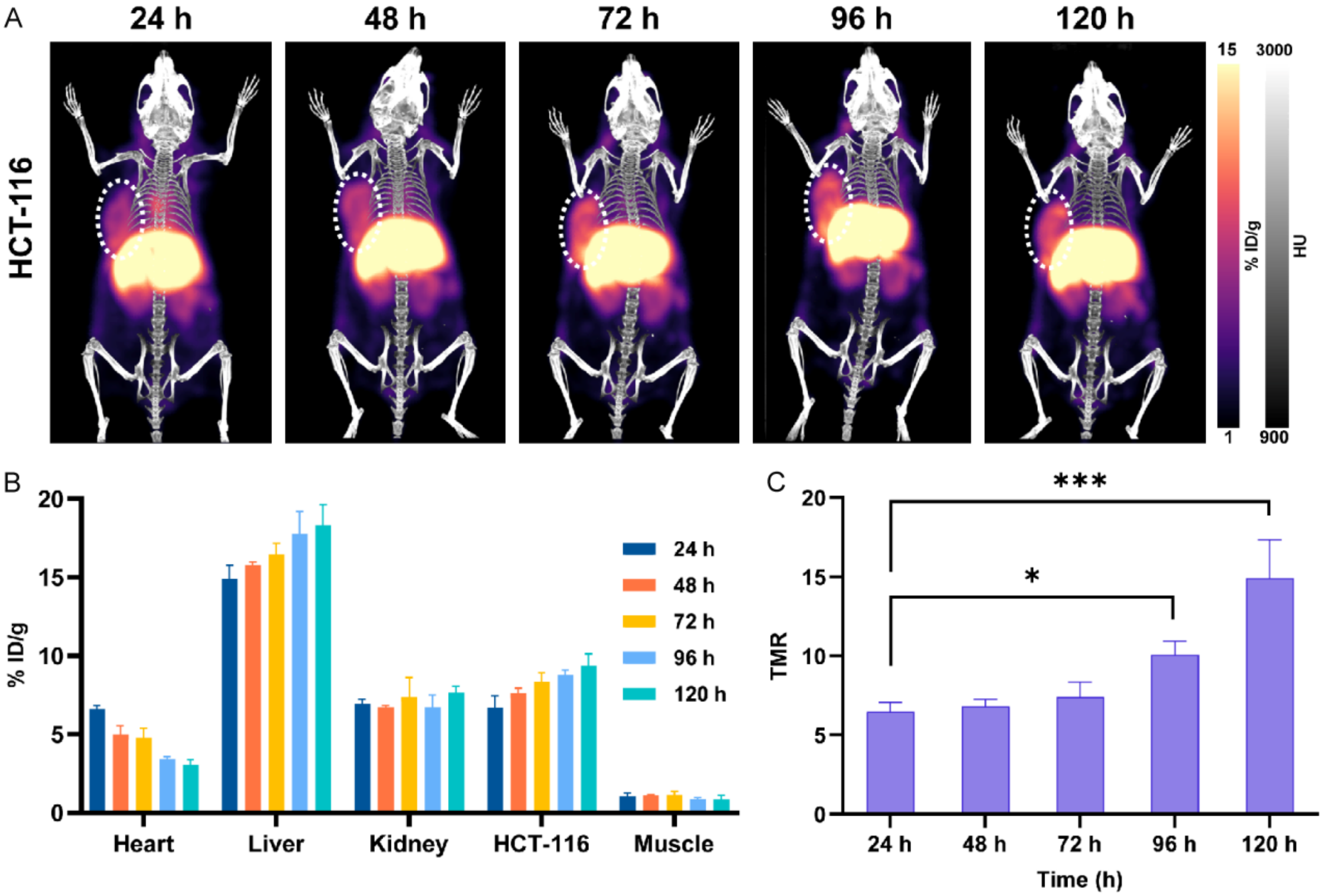

Figure 5. [^{89}Zr]Zr-SN-2D01 immuno-PET/CT imaging in the HCT-116 tumor model. A. Representative PET/CT images of HCT-116 tumor-bearing mice acquired at 24, 48, 72, 96, and 120 h post-injection (p.i.) of [^{89}Zr]Zr-SN-2D01. B. ROI analysis of [^{89}Zr]Zr-SN-2D01 uptake in HCT-116 tumor model. C. Tumor-to-muscle ratio (TMR) of [^{89}Zr]Zr-SN-2D01 in HCT-116 tumor-bearing mice. Data are represented as mean ± SD,$^{*}P < 0.05$, $^{***}P < 0.001$.

delayed imaging. Overall, the PET-derived uptake pattern observed in CRC20-PDX bearing mice was generally consistent with that in the HCT-116 model, characterized by persistent tumor retention, sustained hepatic uptake, decreasing cardiac background activity, and improved tumor delineation at later imaging time points.

Ex vivo biodistribution of [^{89}Zr]Zr-SN-2D01 in HCT-116 and CRC20-PDX tumor models

Ex vivo biodistribution studies of [^{89}Zr]Zr-SN-2D01 were performed in HCT-116 and CRC20-PDX bearing mice at 120 h p.i. (**Figure 7**). In the HCT-116 model, substantial tumor uptake of [^{89}Zr]Zr-SN-2D01 was observed at 120 h p.i., reaching 8.12 ± 1.54 %ID/g. Among the normal tissues examined, the liver showed the highest uptake, with a value of 14.03 ± 2.16 %ID/g, followed by the kidneys at 8.17 ± 1.61 %ID/g. Moderate activity was also detected in the spleen, lungs, and blood, with values of 5.16 ± 1.20, 4.69 ± 2.39, and 4.45 ± 2.06 %ID/g, respectively. In contrast, uptake in the heart, bone, stomach, small intestine, large intestine, pancreas, and muscle remained relatively low. Similarly, in the CRC20-PDX model, [^{89}Zr]Zr-SN-2D01 exhibited prominent tumor accumulation at 120 h p.i., with a value of 11.49 ± 1.32 %ID/g. The liver again displayed the highest uptake among normal organs, reaching 11.74 ± 2.61 %ID/g, whereas renal uptake was measured at 8.60 ± 1.14 %ID/g. Uptake in the spleen, blood, bone, and heart was lower than that in the liver and kidneys, while the gastrointestinal tract, pancreas, and muscle showed comparatively limited tracer retention. Notably, tumor uptake in the CRC20-PDX model was significantly higher than that in the HCT-116 model at the same time point (11.49 ± 1.32 vs 8.12 ± 1.54 %ID/g, $P < 0.05$). Overall, the ex vivo biodistribution data in both models were consistent with the PET/CT imaging findings, demonstrating sustained tumor retention of [^{89}Zr]Zr-SN-2D01 at 120 h p.i., together with relatively high accumulation in the liver and kidneys.

Discussion

The rapid progression of antibody engineering has paved the way for new formats of antibodies. The molecular properties of VHHs hold potential for non-invasive molecular imaging in cancer and other diseases. Several VHH-based agents have progressed into clinical translation

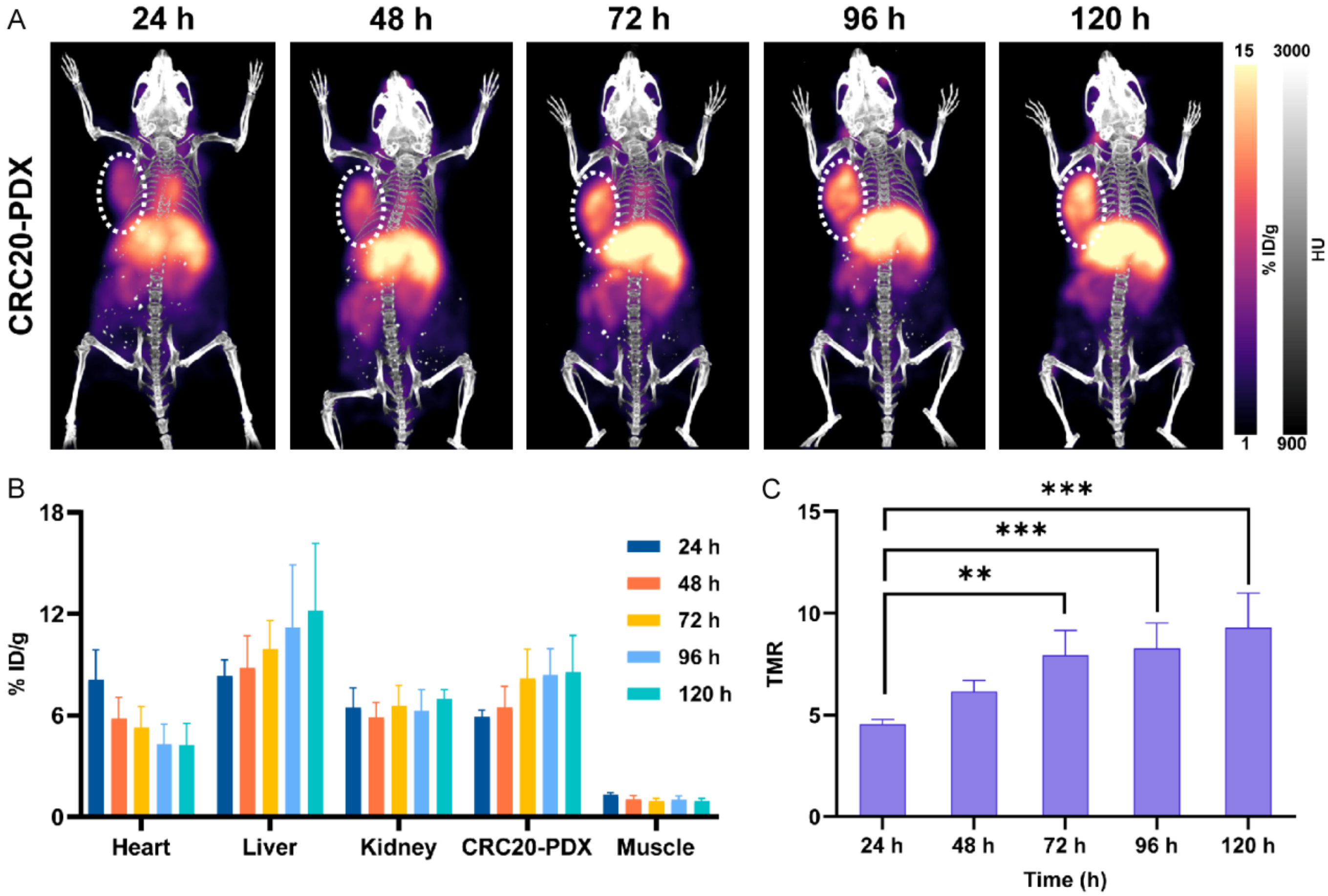

Figure 6. [^{89}Zr]Zr-SN-2D01 immuno-PET/CT imaging in the CRC20-PDX tumor model. A. Representative PET/CT images of CRC20-PDX tumor-bearing mice acquired at 24, 48, 72, 96, and 120 h post-injection (p.i.) of [^{89}Zr]Zr-SN-2D01. B. ROI analysis of [^{89}Zr]Zr-SN-2D01 uptake in CRC20-PDX tumor model. C. Tumor-to-muscle ratio (TMR) of [^{89}Zr]Zr-SN-2D01 in CRC20-PDX tumor-bearing mice. Data are represented as mean ± SD, $^{**}P < 0.01$, $^{***}P < 0.001$.

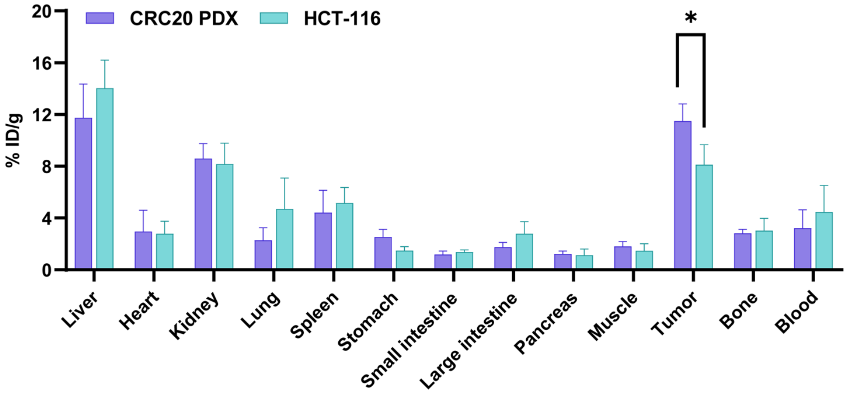

Figure 7. Ex vivo biodistribution of [^{89}Zr]Zr-SN-2D01 in HCT-116 and CRC20-PDX tumor-bearing mice at 120 h p.i. Data are presented as mean ± SD. $^{*}P < 0.05$.

[19, 37-40]. The inherent limitations of VHHs in vivo include relatively low tumor retention and rapid clearance from blood that adversely affects imaging signal-to-noise ratio and overall detection performance. The fusion of VHHs with an ABD through genetic engineering is an effective approach to improve tumour uptake, facilitate a longer circulatory half-life and improve the imaging contrast [41-43], thereby facilitating the development of high-performance targeted imaging probes. In this study, we constructed a PD-L1-targeted VHH-ABD fusion protein, SN-2D01, which was radiolabeled with ^{18}F and ^{89}Zr, respectively. We performed systematic evaluation and compared the performance of these two probes for non-invasive quantification of PD-L1 expression in CRC models, which is expected to lay the rational basis for optimizing PD-L1-directed immunoPET imaging.

In vitro stability assessments demonstrated that [^{18}F]F-SN-2D01and [^{89}Zr]Zr-SN-2D01 maintained excellent radiochemical purity (RCP > 95%) for durations of at least 6 hours and 96 hours, respectively. The results were similar to the favorable stability profiles of other labelled antibodies reported in literature [44, 45]. As ^{18}F is the most commonly used PET radionuclide, it promotes operational practicality in the clinics because of its optimal physical half-life (t1/2 = 118 min) [46, 47]. In this study, ^{18}F-labeled

SN-2D01 was employed to characterize short-term biodistribution in CRC models from 1 to 6 h p.i. Visible tumor accumulation of [^{18}F]F-SN-2D01 was seen as early as 2 h in HCT-116 and CRC20-PDX models, with TMR exceeding 3 at this time point. Over the time, both the tumor uptake and TMR value progressively increased. Moreover, liver and kidney radioactivity levels were less than 10 %ID/g within 6 hours, and heart uptake was less than 20 %ID/g. By contrast, Li et al. have developed the CD70 targeted probe [^{64}Cu]Cu-NOTA-ABDB6, which showed significantly higher initial uptakes in the kidney (~20 %ID/g), liver (~20 %ID/g), and heart (~30 %ID/g) at 1 hour [42]. These results imply that [^{18}F]F-SN-2D01 is primarily eliminated via the renal and hepatobiliary pathways, exhibiting a more favorable normal organ distribution in comparison to the previously reported ABD-conjugated nanobodies.

Given the prolonged blood half-life conferred by ABD conjugation, SN-2D01 was labeled with long-lived radionuclides (e.g., ^{89}Zr, ^{64}Cu) to enable multi-day in vivo distribution profiling. In the present study, we further developed [^{89}Zr]Zr-SN-2D01 and evaluated its performance in CRC models. Serial imaging revealed a progressive increase in tumor uptake over 120 hours, with peak accumulation reaching 8.55 ± 2.18 %ID/g in CRC20-PDX and 9.37 ± 0.76 %ID/g in HCT-116 models, respectively. Correspondingly, TMR in both models approached ~10 at 120 h, supporting high-contrast tumor delineation. Notably, comparative analysis with prior literature highlights the favorable targeting characteristics of [^{89}Zr]Zr-SN-2D01. Cao et al. [48] reported that ^{89}Zr-labeled bispecific antibody ATG-101 (targeting PD-L1/4-1BB) achieved maximal tumor uptake (~10 %ID/g) on day 3, whereas ^{89}Zr-labeled anti-PD-L1 monoclonal antibody showed peak tumor uptake below 10 %ID/g. Similarly, Zhang et al. [41] demonstrated that ^{89}Zr-labeled ABD-fused CD47 nanobody (ABDC2) reached peak tumor accumulation at 72 h. Collectively, these data indicate that the maximum tumor uptake of [^{89}Zr]Zr-SN-2D01 is comparable to that of [^{89}Zr]Zr-anti-PD-L1. However, a key distinction lies in its sustained tumor retention: [^{89}Zr]Zr-SN-2D01 exhibited progressive uptake peaking at 120 h, suggesting that the ABD fusion strategy employed herein more effectively prolongs intratumoral persistence. This property is highly desirable and may translate to improved therapeutic efficacy for future PD-L1-targeted radioimmunotherapy (RIT) applications.

Regarding off-target organ distribution, splenic uptake is a critical consideration due to its association with hematologic toxicity [49]. Over a 10-day monitoring period, [^{89}Zr]Zr-ATG-101 demonstrated persistent splenic accumulation (~10 %ID/g) [48], which may contribute to myelosuppression, such as leukopenia and thrombocytopenia. In contrast, the splenic uptake of [^{89}Zr]Zr-SN-2D01 at 120 h was significantly lower (~5 %ID/g), suggesting a more favorable hematologic safety profile for potential RIT development. However, a notable limitation was identified in hepatic biodistribution: liver uptake of [^{89}Zr]Zr-SN-2D01 gradually increased from 8 %ID/g at 24 h to 17 %ID/g at 120 h. This progressive hepatic accumulation indicates a potential risk of hepatotoxicity, necessitating careful dose optimization and safety monitoring in subsequent RIT studies. To improve clearance and reduce liver uptake, the optimization of chemical structure such as adjusting the isoelectric point or modifying the ABD should be performed in our future study.

In the present study, PD-L1 expression was evaluated in both CRC20-PDX and HCT-116 tumor models. The results confirmed that both models were PD-L1 positive, with higher levels of PD-L1 expression observed in CRC20-PDX tumors compared to HCT-116 tumors. Consistent with this expression profile, biodistribution of [^{89}Zr]Zr-SN-2D01 exhibited significantly higher tumor uptake in CRC20-PDX tumors than in HCT-116 tumors at 120 h p.i. Collectively, these findings demonstrate that [^{89}Zr]Zr-SN-2D01 facilitates the quantitative assessment of PD-L1 expression levels in CRC. However, certain discrepancies were noted between the quantitative data obtained from [^{89}Zr]Zr-SN-2D01 PET imaging and ex vivo biodistribution analysis. The discrepancy between PET-derived ROI quantification and ex vivo biodistribution may be due to partial volume effects, spillover from adjacent tissues, and attenuation correction artifacts, providing context for the small differences observed.

The present study has several limitations which are worth considering. The lack of in vitro assays that determine binding affinities and competitive blocking experiments for [^{89}Zr]Zr-SN-2D01 precludes confirmation of target-specific binding. Also, further studies are needed to assess the relationship between PD-L1 expression levels and the predictive or evaluative capacity of [^{89}Zr]Zr-SN-2D01H in CRC models for immunotherapeutic responses. Furthermore, all these studies were done in athymic nude mice having an incompletely functioning immune system. Because Balb/c-Nude mice lack endogenous T-cells, the baseline PD-L1 expression in these xenografts may differ from that in clinical human tumors, as T-cell-derived cytokines such as interferon-γ, which dynamically modulate PD-L1, are absent. Therefore, future studies are necessary to validate the clinical translation potential of this probe in immunocompetent tumor models to more accurately replicate the tumor immune microenvironment.

Conclusions

We successfully evaluated ^{18}F- and ^{89}Zr-labeled PD-L1-targeting ABD-VHH (SN-2D01) in CRC models. [^{89}Zr]Zr-SN-2D01 had enhanced imaging contrast than [^{18}F]F-SN-2D01. The [^{89}Zr]Zr-SN-2D01 showed promise in noninvasively detecting PD-L1 positive CRC tumors and assessing tissue heterogeneity. Moreover, this non-invasive imaging technique could help identify patients with a response to anti-PD-L1 therapy overcoming the limitations of IHC.

Acknowledgements

Supporting for this research was provided by the National Natural Science Foundation of China (Grant number: 82572269), the Science, Technology and Innovation Commission of Shenzhen Municipality (Grant numbers: JCYJ20220530160213030 and JCYJ2025060418382-1029), Natural Science Foundation of Guangdong Province (Grant number: 2025A1515010950), the Scientific Research Initiation Fund Project of Peking University Shenzhen Hospital (Grant number: KYQD2024402, KYQD-2024432), and the Guangdong Basic Sanming Project of Medicine in Shenzhen (Grant number: SZSM202211037).

Disclosure of conflict of interest

None.

Address correspondence to: Dr. Mengjie Dong, Department of Nuclear Medicine, Peking University Shenzhen Hospital, No. 1120, Lianhua Road, Shenzhen 518036, Guangdong, China. Tel: +86-19832861875; E-mail: Donglab2022@pkuszh.com; Dr. Ling Ding, Department of Epidemiology, School of Public Health, Shanxi Medical University, No. 56, Xinjian South Road, Taiyuan 030001, Shanxi, China. Tel: +86-18835137946; E-mail: dingling79@sxmu.edu.cn

References

[1] Brenner H, Kloor M and Pox CP. Colorectal cancer. Lancet 2014; 383: 1490-1502.

[2] Rocca A, Cipriani F, Belli G, Berti S, Boggi U, Bottino V, Cillo U, Cescon M, Cimino M, Corcione F, De Carlis L, Degiuli M, De Paolis P, De Rose AM, D'Ugo D, Di Benedetto F, Elmore U, Ercolani G, Ettorre GM, Ferrero A, Filauro M, Giuliante F, Gruttadauria S, Guglielmi A, Izzo F, Jovine E, Laurenzi A, Marchegiani F, Marini P, Massani M, Mazzaferro V, Mineccia M, Minni F, Muratore A, Nicosia S, Pellicci R, Rosati R, Russolillo N, Spinelli A, Spolverato G, Torzilli G, Vennarecci G, Viganò L, Vincenti L, Delrio P, Calise F and Aldrighetti L. The Italian Consensus on minimally invasive simultaneous resections for synchronous liver metastasis and primary colorectal cancer: a Delphi methodology. Updates Surg 2021; 73: 1247-1265.

[3] Avella P, Vaschetti R, Cappuccio M, Gambale F, DE Meis L, Rafanelli F, Brunese MC, Guerra G, Scacchi A and Rocca A. The role of liver surgery in simultaneous synchronous colorectal liver metastases and colorectal cancer resections: a literature review of 1730 patients underwent open and minimally invasive surgery. Minerva Surg 2022; 77: 582-590.

[4] Yang Z, Deng W, Zhang X, An Y, Liu Y, Yao H and Zhang Z. Opportunities and challenges of nanoparticles in digestive tumours as anti-angiogenic therapies. Front Oncol 2021; 11: 789330.

[5] Akgül Ö, Çetinkaya E, Ersöz Ş and Tez M. Role of surgery in colorectal cancer liver metastases. World J Gastroenterol 2014; 20: 6113-6122.

[6] Frank MH, Wilson BJ, Gold JS and Frank NY. Clinical implications of colorectal cancer stem cells in the age of single-cell omics and targeted therapies. Gastroenterology 2021; 160: 1947-1960.

[7] Ganesh K, Stadler ZK, Cercek A, Mendelsohn RB, Shia J, Segal NH and Diaz LA Jr. Immunotherapy in colorectal cancer: rationale, challenges and potential. Nat Rev Gastroenterol Hepatol 2019; 16: 361-375.

[8] Biller LH and Schrag D. Diagnosis and treatment of metastatic colorectal cancer: a review. JAMA 2021; 325: 669-685.

[9] Qiu H, Cao S and Xu R. Cancer incidence, mortality, and burden in China: a time-trend analysis and comparison with the United States and United Kingdom based on the global epidemiological data released in 2020. Cancer Commun (Lond) 2021; 41: 1037-1048.

[10] Du W, Frankel TL, Green M and Zou W. IFNγ signaling integrity in colorectal cancer immunity and immunotherapy. Cell Mol Immunol 2022; 19: 23-32.

[11] Schürch CM, Bhate SS, Barlow GL, Phillips DJ, Noti L, Zlobec I, Chu P, Black S, Demeter J, McIlwain DR, Kinoshita S, Samusik N, Goltsev Y and Nolan GP. Coordinated cellular neighborhoods orchestrate antitumoral immunity at the colorectal cancer invasive front. Cell 2020; 182: 1341-1359, e1319.

[12] Wensink E, Bond M, Kucukkose E, May A, Vink G, Koopman M, Kranenburg O and Roodhart J. A review of the sensitivity of metastatic colorectal cancer patients with deficient mismatch repair to standard-of-care chemotherapy and monoclonal antibodies, with recommendations for future research. Cancer Treat Rev 2021; 95: 102174.

[13] Quiroga D, Lyerly HK and Morse MA. Deficient mismatch repair and the role of immunotherapy in metastatic colorectal cancer. Curr Treat Options Oncol 2016; 17: 41.

[14] Lichtenstern CR, Ngu RK, Shalapour S and Karin M. Immunotherapy, inflammation and colorectal cancer. Cells 2020; 9: 618.

[15] André T, Shiu KK, Kim TW, Jensen BV, Jensen LH, Punt C, Smith D, Garcia-Carbonero R, Benavides M, Gibbs P, de la Fouchardiere C, Rivera F, Elez E, Bendell J, Le DT, Yoshino T, Van Cutsem E, Yang P, Farooqui MZH, Marinello P and Diaz LA Jr; KEYNOTE-177 Investigators. Pembrolizumab in microsatellite-instability-high advanced colorectal cancer. N Engl J Med 2020; 383: 2207-2218.

[16] Casak SJ, Marcus L, Fashoyin-Aje L, Mushti SL, Cheng J, Shen YL, Pierce WF, Her L, Goldberg KB, Theoret MR, Kluetz PG, Pazdur R and Lemery SJ. FDA approval summary: pembrolizumab for the first-line treatment of patients with MSI-H/dMMR advanced unresectable or metastatic colorectal carcinoma. Clin Cancer Res 2021; 27: 4680-4684.

[17] Ilie M, Long-Mira E, Bence C, Butori C, Lassalle S, Bouhlel L, Fazzalari L, Zahaf K, Lalvée S, Washetine K, Mouroux J, Vénissac N, Poudenx M, Otto J, Sabourin JC, Marquette CH, Hofman V and Hofman P. Comparative study of the PD-L1 status between surgically resected specimens and matched biopsies of NSCLC patients reveal major discordances: a potential issue for anti-PD-L1 therapeutic strategies. Ann Oncol 2016; 27: 147-153.

[18] Patel SP and Kurzrock R. PD-L1 expression as a predictive biomarker in cancer immunotherapy. Mol Cancer Ther 2015; 14: 847-856.

[19] Ma X, Hu B, Zhou X, Wang L, Chen H, Xie F, Zhu H, Jia B and Yang Z. Development and first-in-human evaluation of a site-specific [(18)F]-labeled PD-L1 nanobody PET radio-

tracer for noninvasive imaging in NSCLC. Bioorg Chem 2025; 156: 108222.

[20] Bansal A, Lavoie RR, Lucien F, Kethamreddy M, Wootla B, Dong H, Park SS and Pandey MK. Synthesis and evaluation of anti-PD-L1-B11 antibody fragments for PET imaging of PD-L1 in breast cancer and melanoma tumor models. Sci Rep 2024; 14: 19561.

[21] Brown EL, DeWeerd RA, Zidel A and Pereira PMR. Preclinical antibody-PET imaging of PD-L1. Front Nucl Med 2022; 2: 953202.

[22] Zhou X, Jiang J, Yang X, Liu T, Ding J, Nimmagadda S, Pomper MG, Zhu H, Zhao J, Yang Z and Li N. First-in-humans evaluation of a PD-L1-binding peptide PET radiotracer in non-small cell lung cancer patients. J Nucl Med 2022; 63: 536-542.

[23] Niemeijer AN, Leung D, Huisman MC, Bahce I, Hoekstra OS, van Dongen GAMS, Boellaard R, Du S, Hayes W, Smith R, Windhorst AD, Hendrikse NH, Poot A, Vugts DJ, Thunnissen E, Morin P, Lipovsek D, Donnelly DJ, Bonacorsi SJ, Velasquez LM, de Gruijl TD, Smit EF and de Langen AJ. Whole body PD-1 and PD-L1 positron emission tomography in patients with non-small-cell lung cancer. Nat Commun 2018; 9: 4664.

[24] Giesen D, Broer LN, Lub-de Hooge MN, Popova I, Howng B, Nguyen M, Vasiljeva O, de Vries EGE and Pool M. Probody therapeutic design of (89)Zr-CX-072 promotes accumulation in PD-L1-expressing tumors compared to normal murine lymphoid tissue. Clin Cancer Res 2020; 26: 3999-4009.

[25] Kist de Ruijter L, Hooiveld-Noeken JS, Giesen D, Lub-de Hooge MN, Kok IC, Brouwers AH, Elias SG, Nguyen MTL, Lu H, Gietema JA, Jalving M, de Groot DJA, Vasiljeva O and de Vries EGE. First-in-human study of the biodistribution and pharmacokinetics of 89Zr-CX-072, a novel immunopet tracer based on an anti-PD-L1 probody. Clin Cancer Res 2021; 27: 5325-5333.

[26] Bensch F, van der Veen EL, Lub-de Hooge MN, Jorritsma-Smit A, Boellaard R, Kok IC, Oosting SF, Schröder CP, Hiltermann TJN, van der Wekken AJ, Groen HJM, Kwee TC, Elias SG, Gietema JA, Bohorquez SS, de Crespigny A, Williams SP, Mancao C, Brouwers AH, Fine BM and de Vries EGE. (89)Zr-atezolizumab imaging as a non-invasive approach to assess clinical response to PD-L1 blockade in cancer. Nat Med 2018; 24: 1852-1858.

[27] Jagoda EM, Vasalatiy O, Basuli F, Opina ACL, Williams MR, Wong K, Lane KC, Adler S, Ton AT, Szajek LP, Xu B, Butcher D, Edmondson EF, Swenson RE, Greiner J, Gulley J, Eary J and Choyke PL. Immuno-PET imaging of the programmed cell death-1 Ligand (PD-L1) using a Zirconium-89 labeled therapeutic antibody, avelumab. Mol Imaging 2019; 18: 1536012119829986.

[28] Smit J, Borm FJ, Niemeijer AN, Huisman MC, Hoekstra OS, Boellaard R, Oprea-Lager DE, Vugts DJ, van Dongen GAMS, de Wit-van der Veen BJ, Thunnissen E, Smit EF and de Langen AJ. PD-L1 PET/CT imaging with radiolabeled durvalumab in patients with advanced-stage non-small cell lung cancer. J Nucl Med 2022; 63: 686-693.

[29] Chakravarty R, Goel S and Cai W. Nanobody: the “magic bullet” for molecular imaging? Theranostics 2014; 4: 386-398.

[30] Cong Y, Devoogdt N, Lambin P, Dubois LJ and Yaromina A. Promising diagnostic and therapeutic approaches based on VHHs for cancer management. Cancers (Basel) 2024; 16: 371.

[31] Xing Y, Chand G, Liu C, Cook GJR, O’Doherty J, Zhao L, Wong NCL, Meszaros LK, Ting HH and Zhao J. Early phase I study of a (99m)Tc-labeled anti-programmed death ligand-1 (PD-L1) single-domain antibody in SPECT/CT assessment of PD-L1 expression in non-small cell lung cancer. J Nucl Med 2019; 60: 1213-1220.

[32] Ma X, Zhou X, Hu B, Li X, Yao M, Li L, Qin X, Li D, Yao Y, Hou X, Liu S, Chen Y, Wang Z, Zhou W, Li N, Zhu H, Jia B and Yang Z. Preclinical evaluation and pilot clinical study of [(68)Ga]Ga-THP-APN09, a novel PD-L1 targeted nanobody radiotracer for rapid one-step radiolabeling and PET imaging. Eur J Nucl Med Mol Imaging 2023; 50: 3838-3850.

[33] Zhang Y, Cao M, Wu Y, Malih S, Xu D, Yang E, Younis MH, Lin W, Zhao H, Wang C, Liu Q, Engle JW, Rasaee MJ, Guan Y, Huang G, Liu J, Cai W, Xie F and Wei W. Preclinical development of novel PD-L1 tracers and first-in-human study of [(68)Ga]Ga-NOTA-RW102 in patients with lung cancers. J Immunother Cancer 2024; 12: e008794.

[34] Zhang S, Wang X, Gao X, Chen X, Li L, Li G, Liu C, Miao Y, Wang R and Hu K. Radiopharmaceuticals and their applications in medicine. Signal Transduct Target Ther 2025; 10: 1.

[35] Leekens S, Casteels P, Van Bogaert T, Deschaght P, De Brabandere V, Cawthorne C, Bormans G and Cleeren F. Affinity- and format-dependent pharmacokinetics of (89)Zr-labeled albumin-binding VHH constructs. Pharmaceuticals (Basel) 2026; 19: 120.

[36] D’Huyvetter M, Vos J, Caveliers V, Vaneycken I, Heemskerk J, Duhoux FP, Fontaine C, Vanhoeij M, Windhorst AD, Aa FV, Hendrikse NH, Eersels JLE, Everaert H, Gykiere P, Devoogdt N, Raes G, Lahoutte T and Keyaerts M. Phase I trial of (131)I-GMIB-Anti-HER2-VHH1, a new promising candidate for HER2-targeted radionuclide therapy in breast cancer patients. J Nucl Med 2021; 62: 1097-1105.

[37] Qi C, Guo R, Chen Y, Li C, Liu C, Zhang M, Zhang C, Zhang X, Hou X, Chen B, Jia B, Yang Z, Shen L and Zhu H. (68)Ga-NC-BCH whole-body PET imaging rapidly targets claudin18.2 in lesions in gastrointestinal cancer patients. J Nucl Med 2024; 65: 856-863.

[38] Zhou X, Wu Q, Zhai W, Zhang Y, Wu Y, Cao M, Wang C, Guan Y, Liu J, Xie F and Wei W. CD70-targeted immuno-PET/CT imaging of clear cell renal cell carcinoma: a translational study. J Nucl Med 2024; 65: 1891-1898.

[39] Zhang L, Zhou M, Lu C, Zhao P, Shi N, Zhou Y, Yao C, Yang X, Tian J, Wang J, Ma Y, Huang Q, Xu C, Gao P, Zhou W, Hu S and Luo L. A high-affinity CEA-targeted nanobody for (68)Ga PET imaging and (177)Lu-based radioisotope therapy: preclinical and first-in-human evaluation. J Nanobiotechnology 2025; 23: 734.

[40] Huang W, Zhang Y, Cao M, Wu Y, Jiao F, Chu Z, Zhou X, Li L, Xu D, Pan X, Guan Y, Huang G, Liu J, Xie F and Wei W. ImmunoPET imaging of Trop2 in patients with solid tumours. EMBO Mol Med 2024; 16: 1143-1161.

[41] Zhang Y, Zhang D, An S, Liu Q, Liang C, Li J, Liu P, Wu C, Huang G, Wei W and Liu J. Development and characterization of nanobody-derived CD47 theranostic pairs in solid tumors. Research (Wash D C) 2023; 6: 0077.

[42] Li X, Zhang Y, Mixdorf JC, Wu Q, Lee SJ, Engle JW, Barnhart TE, Kenney SC, Rui L, Wei W and Cai W. Development and preclinical evaluation of [(64)Cu]Cu-NOTA-ABDB6: a CD70 and albumin dual-binding tracer with improved pharmacokinetics. J Nucl Med 2025; 66: 552-558.

[43] Hu G, Zhu W, Liu Y, Wang Y, Zhang Z, Zhu S, Duan W, Zhou P, Fu C, Li F and Huo L. Development and comparison of

three (89)Zr-labeled anti-CLDN18.2 antibodies to noninvasively evaluate CLDN18.2 expression in gastric cancer: a preclinical study. Eur J Nucl Med Mol Imaging 2022; 49: 2634-2644.

[44] Krache A, Fontan C, Pestourie C, Bardiès M, Bouvet Y, Payoux P, Chatelut E, White-Koning M and Salabert AS. Preclinical pharmacokinetics and dosimetry of an (89)Zr labelled anti-PDL1 in an orthotopic lung cancer murine model. Front Med (Lausanne) 2021; 8: 741855.

[45] Massicano AVF, Song PN, Mansur A, White SL, Sorace AG and Lapi SE. [(89)Zr]-Atezolizumab-PET imaging reveals longitudinal alterations in PDL1 during therapy in TNBC preclinical models. Cancers (Basel) 2023; 15: 2708.

[46] Li X, Lu N, Lin L, Chen Y, Yang S, Wang H, Liu X, Wu C, Xue X, Su X, Bai X and Liang T. (18)F-FAPI-04 outperforms (18) F-FDG PET/CT in clinical assessments of patients with pancreatic adenocarcinoma. J Nucl Med 2024; 65: 206-212.

[47] Gillett D, MacFarlane J, Goodchild E, Wu X, Kearney J, Laycock K, Leek F, Crawford R, Spink S, Senanayake R, Harper I, Mendichovszky IA, Aloj L, Cheow H, Aigbirhio FI, Drake WM, Brown MJ and Gurnell M. Voxel-level comparison of [(18)F]CETO and [(11)C]MTO for molecular imaging of primary aldosteronism. J Nucl Med Technol 2025; 53: 312-317.

[48] Cao Z, Wichmann CW, Burvenich IJG, Osellame LD, Guo N, Rigopoulos A, O'Keefe GJ, Scott FE, Lorensuhewa N, Lynch KP and Scott AM. Radiolabelling and preclinical characterisation of [(89)Zr]Zr-Df-ATG-101 bispecific to PD-L1/4-1BB. Eur J Nucl Med Mol Imaging 2024; 51: 3202-3214.

[49] Gagelmann N, Hobbs GS, Campodonico E, Helbig G, Novak P, Schroeder T, Schneider A, Rautenberg C, Reinhardt HC, Bosques L, Heuser M, Panagiota V, Thol F, Gurnari C, Maciejewski JP, Ciceri F, Rathje K, Robin M, Pagliuca S, Rubio MT, Rocha V, Funke V, Hamerschlak N, Salit R, Scott BL, Duarte F, Mitrus I, Czerw T, Greco R and Kröger N. Splenic irradiation for myelofibrosis prior to hematopoietic cell transplantation: a global collaborative analysis. Am J Hematol 2024; 99: 844-853.